Journal of Ultrafine Grained and Nanostructured Materials
https://jufgnsm.ut.ac.ir
Vol. 58, No.1, June 2025, pp. 67-77
Print ISSN: 2423-6845 Online ISSN: 2423-6837
DOI: 10.22059/jufgnsm.2025.01.07

Corrosion behavior of ultrasonic impact treated Haynes 25 superalloy

Rahim Nemati[1], Reza Taghiabadi[1*], Morteza Saghafi Yazdi[1], Saeid Amini[2]

[1]Department of Materials Science and Engineering, Imam Khomeini International University, Qazvin, Iran
[2]Department of Manufacturing and Production, Faculty of Mechanical Engineering, University of Kashan, Kashan, Iran

Recieved: 27 March 2025; Accepted: 16 April 2025

[*]Corresponding author, E-mail: taghiabadi@ikiu.ac.ir

ABSTRACT

The effect of ultrasonic impact treatment (UIT) was studied on the microstructure and corrosion behavior of Haynes 25 superalloy. The UIT was performed at a frequency of 20 kHz, tool feeding rates of 0.08, 0.12, and 0.16 mm/rev, vibration amplitudes of 10, 28, and 50% of the machine power, static pressures of 0.1 and 0.9 bar at the different number of passes (one, two, three, five, and seven). According to the results, the UIT severely deformed the surface layers up to a depth of about 100 µm and promoted the emergence of deformation bands/strain-induced martensite (ε-phase) up to a depth of about 400 µm. The UIT also produced ultrafine grain structure in the surface region and due to the deformation inhomogeneity developed surface compressive residual stresses. The Tafel polarization tests indicated that applying one pass UIT at the static pressures of 0.1 and 0.9 bar reduced the corrosion current (from 4.16 µA/cm^2 to 1.3 µA/cm^2 and 2.18 µA/cm^2, respectively), and the corrosion potential (from -0.6 V to -0.7 V and -0.8 V, respectively). This behavior was found to be due to promotion of surface oxidation and formation of protective layer on the surface. Despite increasing the surface smoothness, further increasing the UIT pass number to seven, probably due to encouraging the formation of surface pits/microcracks increased the corrosion current and corrosion rate by about 45%. According to the electrochemical impedance tests, at the static pressure of 0.9 bar, the as-received and seven-pass UITed samples showed the lowest corrosion resistance whilst one-pass and two-pass UITed samples revealed the highest corrosion resistance. The effect of tool feeding rate on the corrosion resistance was found to be minor.

Keywords: *Haynes 25, Superalloy, Ultrasonic impact treatment, Severe plastic deformation, Corrosion.*

1. Introduction

Haynes 25 (L-605), is a wear-, corrosion- and heat-resistant CoCrWNi superalloy which is widely used in applications such as gas turbines and the aerospace industry due to its high strength at high temperatures and excellent resistance to oxidation (up to about 1100 °C). Haynes 25 is also used in the production of surgical implants such as hip implants, surgical fixation wires, cerclage suture wires, orthopedic wires, heart valves, and stents due to its excellent corrosion resistance and proved biocompatibility in the body environment [1,2].

However, the application of CoCr-based alloys as implant may face some challenges. For instance, the occurrence of wear and corrosion, due to releasing Cr and Co ions into the body environment, may cause adverse biological reactions and toxic effects [3]. Therefore, surface improvement processes such as electrochemical polishing, ion implantation, ultrasonic polishing, and laser processing have been widely proposed to modify the surface roughness and improve the tribological properties and corrosion resistance of these alloys. Strain-induced martensitic transformation is one of the most attractive features of CoCr-based alloys whereby they can be easily hardened by cold working.

Indeed, due to the low stacking fault energy of Co limited cross-slip of dislocations is likely to be occurred in the deformed crystal structure of the alloy increasing the fraction of deformation twins and HCP martensite within its structure. This disrupts the motion of dislocation and, accordingly, promotes its severe work hardening [4]. Therefore, surface severe plastic deformation (S^2PD) processes are thought to be a suitable option for creating microstructural changes and consequently improving surface properties of Haynes 25 alloy.

One of the relatively new processes based on S^2PD is UIT which is also known as ultrasonic cold forging technology (UCFT), ultrasonic peening technology (UPT), ultrasonic nanocrystalline surface modification (UNSM) [5], and ultrasonic-assisted constraint groove pressing [6]. This process was first proposed in 2001 by Cho et al. as an efficient plastic deformation method for improving the hardness, surface smoothness, and toughness of engineering alloys [7]. In UIT, the surface is subjected to repeated impacts of a hard spherical tool where the subsurface layers reach their yield point and severe plastic deformation occurs [8,9].

Like other S^2PD processes, applying UIT can affect the surface structure of the material through microstructural densification, formation of ultrafine grains (increasing the density of grain boundaries), changing the crystallographic texture, encouraging strain-induced phase transformations, accumulation of plastic strain, increasing the number of dislocations, and developing compressive residual stresses, which in turn changes surface properties such as tribological properties and corrosion resistance [10,11]. Grain boundaries are high energy planar defects which increase the diffusion coefficient, reduce the atomic coordination number, and increase the activity of electrons [12]. According to the Palumbo's estimation, in a material with an average grain size of 2 nm, about 90% of atoms are located at the grain boundaries [13]. Splinter et al. also showed that reducing the coordination number in nanostructured materials reduces the surface work function and increases the possibility of adsorption of various species from the corrosive solution or possibly increases the rate of charge transfer [14]. Therefore, a sharp increase in the density of boundaries in the SPDed region is likely to increase the surface reactivity. Cold working may also increase or decrease the corrosion rate of pure metals depending on the crystallographic texture created [15]. Lee and White attributed the change in corrosion behavior with change in surface texture to the density of surface atoms. They showed that changing the crystal orientation, changes the number of existing atoms affecting the reaction kinetics [16].

Various researchers studied the effect of UIT on the corrosion resistance of industrial alloys. However, despite the unique properties and practical importance of Haynes 25 superalloy, no targeted research has been conducted so far on the effect of UIT on its corrosion behavior. In one of the few studies, Petrov et al. investigated the effect of ultrasonic impact peening (UIP) on the corrosion properties of a CoCrMo alloy. They showed that applying the UIP increases the oxygen concentration at the surface and nobles the potential from -406 mV to -300 mV [17]. In another study, Kim Kita et al. reported the positive impact of the ultrasonic peening by UNSM on the corrosion resistance of Inconel 600 superalloy [18]. In view of the above, in the present study, an attempt has been made to investigate the effect of UIT parameters on the microstructure and corrosion behavior of Haynes 25 superalloy.

2. Materials and methods

The samples of the present study were prepared from 6 mm thick Haynes 25 superalloy sheet. The sheets were produced by melting route in a vacuum induction melting furnace followed by electroslag refining, hot rolling, solution annealing at 1180 °C for two hours, and quenching in room temperature water. The chemical composition of the sheet (determined by atomic absorption spectrometry) is presented in Table 1.

An overview of the equipment used for the UIT, including a lathe, pneumatic pressure system, and vibrating tool, is shown in Fig. 1. An MPI-3KW model generator with a power of 3 kW and a frequency range of 18-30 kHz capable of vibration amplitude control was used to generate ultrasonic waves. The UIT was performed at tool feeding rates of 0.08, 0.12, and 0.16 mm/rev, static pressures of 0.1 and 0.9 bar (equivalent to 0.01 and 0.09 MPa), vibration amplitudes of 10% and 28% of the machine power, for one, two, three, five, and seven passes. Based on our preliminary experiments, the

Table 1- Chemical composition of the experimental Haynes 25 superalloy, wt. %

Co	Cr	W	Ni	Fe	Mn	Si	C	P	S
Base	19.46	14.1	10.14	3.67	1.07	0.18	0.06	0.008	0.001

best vibration condition was achieved at vibration amplitude of 28% and was thus used in our investigation. The samples were coded as xUITX-X-X based on the process parameters. The digit before the UIT indicates the number of passes, the first digit after the UIT indicates the percentage of vibration amplitude, the second digit indicates the tool feeding rate from edge to center (in mm/rev), and the last digit indicates the pressure of the pneumatic system (in bar).

For metallographic studies, the surface of samples was prepared using standard metallographic methods in accordance with ASTM E3-11. The surface preparation was carried out using P280, P400, P800, P1500 and P3000 abrasive papers followed by polishing with 0.1 μm diamond paste. The surface was then chemically etched using a solution consisting of HCl and H_2O_2 with a volumetric mixing ratio of 20 to 1. An optical microscope (OM, Olympus BX51) and a field emission scanning electron microscope (FESEM, MIRA3 TESCAN) equipped with an energy dispersive spectroscopy (EDS) detector were used to examine the microstructure and elemental analysis of samples.

The X-ray diffraction (XRD) pattern of samples was also collected using Cu K-α radiation with the angle range and scanning time of 2θ = 0.02 and 0.8 s, respectively. The residual stress of samples was measured using the $Sin^2\psi$ method in accordance with DIN EN 15305-2009. More details can be found in [19]. The three-dimensional surface roughness profile of samples was obtained using an atomic force microscope (AFM, NanoScope III, Digital Instruments).

The corrosion behavior of samples in the simulator body fluid (SBF) was investigated with direct and alternating currents using an Ivium Labview device. Electrochemical Tafel and electrochemical impedance spectroscopy (EIS) experiments were performed in an electrochemical cell consisting of three electrodes including a saturated calomel reference electrode (three mole saturated potassium per liter of distilled water), a working electrode (Haynes 25 sample), and a counter electrode (Pt), and their Tafel and impedance curves were plotted. Samples were prepared according to ASTM G5 by abrasive paper P600. Before all experiments, to create stable conditions in the open circuit potential, the working electrode was exposed to the solution for 1 h so that the initial reactions of the solution with the sample reached a stable state and equilibrium open circuit potential was created.

3. Results and Discussion

3.1. Effect of UIT on microstructural characteristics of Haynes 25 superalloy

The FESEM image showing the microstructure of Haynes 25 superalloy in the annealed condition and the corresponding XRD pattern are presented in Fig. 2a and 2b, respectively. As can be seen, the initial structure of the alloy consists of γ-FCC grains and twins resulting from the annealing process. Annealing twins are usually formed in recrystallized microstructure through grain growth or grain boundary dissociation processes [20]. Based on the image analysis results, the average grain size of the alloy was determined to be about 150 ± 52 μm.

OM and FESEM micrographs showing the cross-section microstructure of the one-pass UITed alloy (1UIT28-0.08-0.1 sample) are shown in Fig. 3a and Fig. 3b, respectively. Moreover, in order to better examine the UIT effect on the different areas on the alloy cross-section, high magnification FESEM micrographs are also provided in Fig. 3c and Fig. 3d which are corresponding to the severe plastically deformed (SPD) and plastically deformed (PD) regions in Fig. 3b, respectively.

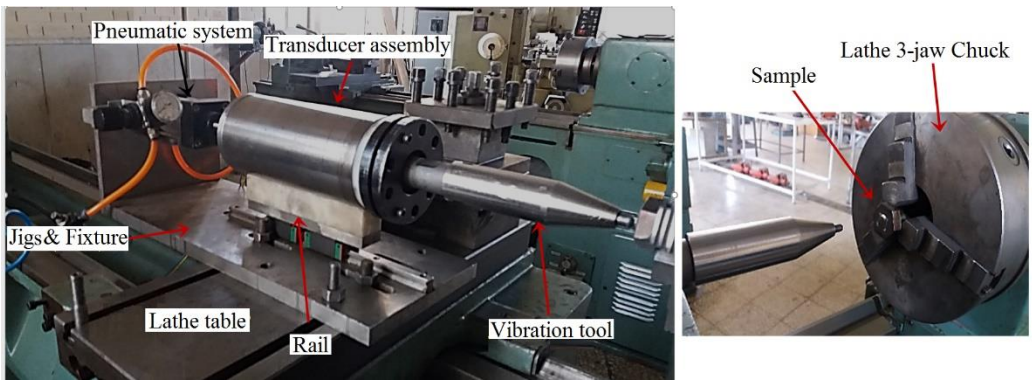

Fig. 1- Overview of the UIT equipment assembled on a lathe.

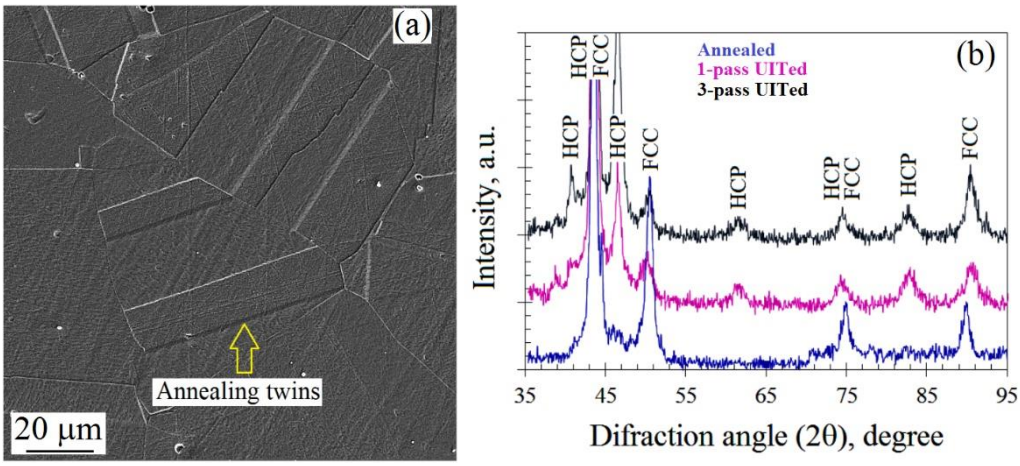

Fig. 2- (a) FESEM image showing the microstructure of the Haynes 25 superalloy in the annealed condition and (b) XRD patterns of the alloy in the annealed and UITed conditions (one and three passes).

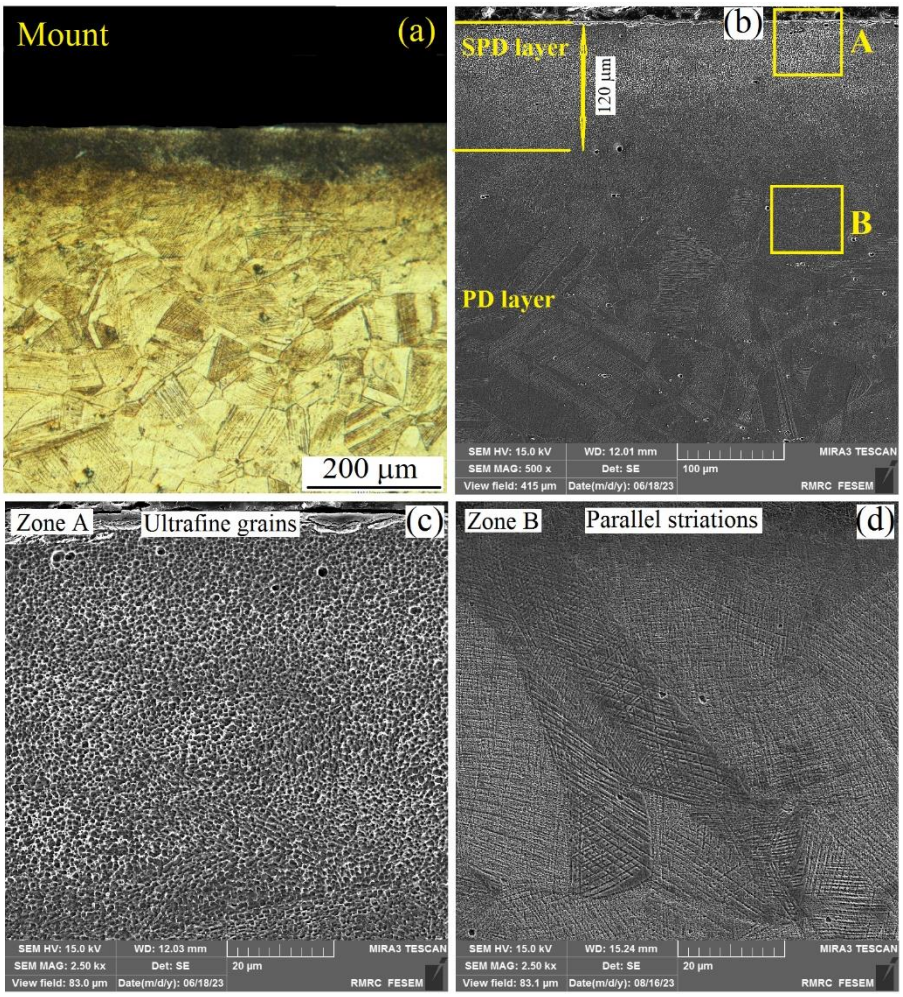

Fig. 3- (a) OM image and (b-d) FESEM images showing the cross-sectional microstructure of Haynes 25 superalloy after one-pass UIT, (c) and (d) higher magnification FESEM images corresponding to the zones A and B in micrograph 3b.

As can be seen, up to a depth of about 400 μm from the UITed surface, two distinct regions are visible: the SPD region (up to a depth of about 100 μm from the processed surface) and PD region (up to a depth of about 400 μm from the processed surface). Probably due to the intense/complex material flow, no distinct microstructural feature/grain structure can be identified within the SPD layer. The formation of ultrafine and equiaxed micro-holes in this region (Fig. 3c) can be attributed to the sharp increase in the density of dislocations and formation of an ultrafine-grained microstructure which exhibits strong reaction with the etching solution. Examination and comparison of crystallite size using the Williamson-Hall method (XRD peak broadening) indicates that by increasing the number of UIT passes from one to two and three, the crystallite size decreased from 38 nm to 19 and 14 nm.

The microscopic structure of the PD region (Fig. 3d) consists of deformation bands in the form of parallel and intersecting lines, which are probably appeared due to the low stacking fault energy of Co and the occurrence of shear martensitic transformation induced by plastic deformation. The effect of plastic strains on the development of deformation bands (martensite formation) has been previously investigated by various researchers, including the development of these bands in Inconel 600 [18] and 304 stainless steel [21] after surface mechanical attrition treatment (SMAT), Co-20Cr alloy after hot rolling (HR) [22] and CoCrW alloy [23].

The XRD patterns of one- and three-pass UITed samples (xUIT28-0.08-0.9) are presented in Fig. 2b. The diffraction peaks at the angles 2θ of 43°, 51°, 75° and 91° correspond to the (111), (200), (220) and (311) crystal planes, respectively. These are consistent with the standard peaks reported for the FCC-structured Co-based samples. Examining the standard diffraction peaks corresponding to the FCC- and HCP-structured Co also reveals that the diffraction peak at 2θ = 51° belongs to the FCC crystal lattice and the diffraction peaks at 2θ = 41°, 47°, 62° and 83° belong to the HCP crystal lattice. The peaks at the 2θ angles of 43°, 75° and 91° are also common to both crystal structures.

Therefore, it seems that UIT caused the emergence of new peaks specific to the HCP crystal structure, while decreased the intensity of the characteristic peak of the FCC crystal lattice. This confirms a strain-induced martensitic transformation during which the FCC phase is partially converted to the HCP phase. It is also evident form the XRD patterns that an increase in the number of passes, increases the peaks intensity of the HCP phase at the 2θ angles of 41° and 47° which are related to the {010} and {011} planes, respectively and lowers the peak intensity at the 2θ angels of 51° related to the FCC phase. Similar results were obtained in the research work made by Zhu et al. [24] on the L-605 alloy. They showed that at low cold work levels, small-angle twin boundaries are responsible for the formation of HCP phase whilst at the higher cold work intensities (about 30%), probably due to the rotation of large-angle twin boundaries, large-angle grain boundaries are emerged and act as nucleation sites for the HCP phase. Also, at 40% cold work, HCP phase is formed inside the grains.

Another consequence of UIT is the development of compressive surface residual stresses. Based on calculations made using the $Sin^2\psi$ method, applying the first pass of UIT changes the surface tensile residual stress in the as-received sample (175±84 MPa) to compressive residual stress. Typical residual stress values for selected samples are presented in Table 2. As can be seen, increasing the number of UIT passes, decreasing the tool feeding rate, and increasing the static load, all increase the amount of compressive surface residual stress, probably due to the increase in surface strains applied. This is in line with the previous reports on the proportionality between the amount of compressive surface residual stress and the number of UIT passes in Inconel 690 and 718 alloys [25]. The emergence of surface residual stress in the UITed samples is thought to be due to the deformation inhomogeneity in surface layers. Indeed, despite very high plastic strain applied on the outermost layers, substantially lower strains is applied on the lower layers where elastic deformation occurs.

Table 2- Residual stress values of selected samples determined by the $Sin^2\psi$ method at an angle of 147°

Sample code	Residual stress (MPa)
As-received	175±89
1UIT28-0.08-0.1	-195±71
1UIT28-0.08-0.9	-305±46
2UIT28-0.08-0.9	-580±74
5UIT28-0.08-0.1	-370±88
2UIT28-0.12-0.9	-210±39
3UIT28-0.12-0.9	-790±92

The low and elastic deformation of lower layers significantly restricts the free plastic deformation of surface layers causing the surface tensile stress convert into compressive sign. After unloading, compressive residual stress is created at the surface and tensile residual stress is created below the surface [26].

3.2. Effect of UIT on corrosion behavior of Haynes 25 superalloy

The Tafel polarization diagrams of the as-received (annealed) and selected UITed samples with different tool feeding rate, static pressure, and number of passes are shown in Fig. 4. The values obtained from the curves including corrosion current, corrosion rate, corrosion potential, and polarization resistance are presented in Table 3. According to the results (Fig. 4), UIT generally increases the corrosion resistance of Haynes 25 superalloy. However, reducing the process static pressure from 0.9 to 0.1 bar and increasing the number of process passes (from one to seven) has a negative effect on the corrosion resistance. Also, the effect of tool feeding rate on the corrosion resistance of the samples is minor.

Comparing the Tafel analysis results of the as-received and 1UIT28-0.08-0.1 and 1UIT28-0.08-0.9 samples indicates that applying one pass UIT at static pressures of 0.1 and 0.9 bar reduced the corrosion current from 4.16 μA/cm^2 to 3.1 μA/cm^2 and 2.18 μA/cm^2 and reduced the corrosion potential from -0.6 V to -0.7 V and -0.8 V,

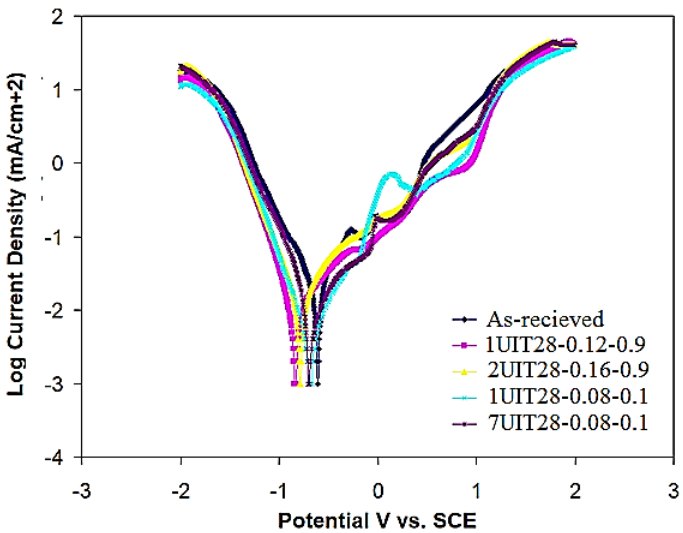

Fig. 4- Tafel polarization corrosion test curves of the as-received and selected UITed samples.

Table 3- Summary of Tafel polarization test results of the as-received and UITed samples presented in Fig. 4

Sample code	$I_{Corr.}$ (μA/cm^2)	$E_{Corr.}$ (V)	R_p (ohm)	Corrosion rate (μm/year)
Base	4.16	-0.6	4299	13.6
1UIT28-0.08-0.1	3.1	-0.7	7002	10.1
3UIT28-0.08-0.1	3.87	-0.7	7205	10.9
7UIT28-0.08-0.1	4.47	-0.71	7496	14.6
1UIT28-0.08-0.9	2.18	-0.8	9342	7.5
1UIT28-0.12-0.9	1.92	-0.83	9688	6.2
2UIT28-0.16-0.9	1.96	-0.78	8484	6.4

respectively. Moreover, comparing the Tafel analysis results of 1UIT28-0.08-0.1 and 2UIT28-0.16-0.9 samples, reveals that increasing UIT static pressure from 0.1 to 0.9 bar decreased the corrosion rate and the corrosion potential from 10.4 µm/year to 1.6 µm/year and from -0.7 V to -0.78 V, respectively, and moved the corrosion potentials to the more noble values. It is worth noting that the number of ultrasonic impacts per unit area in two-pass UITed sample (0.16 mm/rev) and one-pass UITed sample (0.08 mm/rev) are equal.

It seems that increasing the dislocations density, reduction of grain size, and the development of residual stresses on the surface of UITed samples are the main factors responsible for increasing their corrosion resistance [27,28]. This is because they are likely to increase the free energy/activity of the surface, promote surface oxidation, and encourage the formation of protective layer on the sample surface. Increasing the grain boundary density also increases the adherence of surface oxide film to the substrate. This arises from the fact that the grain boundaries serve as fast diffusion pathways, enhance the electrons activity and promote the pegging mechanism [29]. Local heating of the sample surface during the process also helps to absorb oxygen and accelerate oxidation.

The distribution of oxygen element on the surface of the as-received, one-pass UITed and three-pass UITed samples (Fig. 5a-5c) implies significant growth in the surface oxygen concentration in the course of UIT. Despite its low accuracy in detection of the relatively light atoms, the EDS analyses (Fig. 6) also reveal significant increase in the oxygen content upon UIT or equivalently the formation of protective oxide layers on the surface of UITed samples. Petrov et al. also reported an increase in oxygen concentration on the surface of a CoCrMo alloy due to the UIP with a tool frequency of 21.7 kHz [17].

Kim et al. confirm an increase in the polarization resistance of Inconel 600 alloy due to increasing the UIT static pressure up to a critical level. They

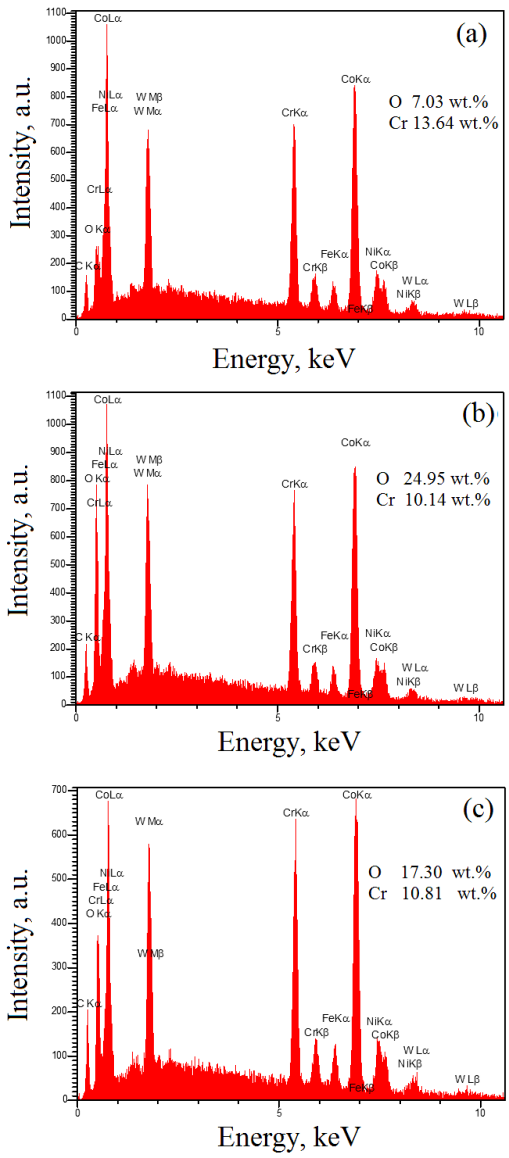

Fig. 6- EDS analyses corresponding to the surface of the experimental sample (a) as-received, (b) one-pass UITed, and (c) three-pass UITed.

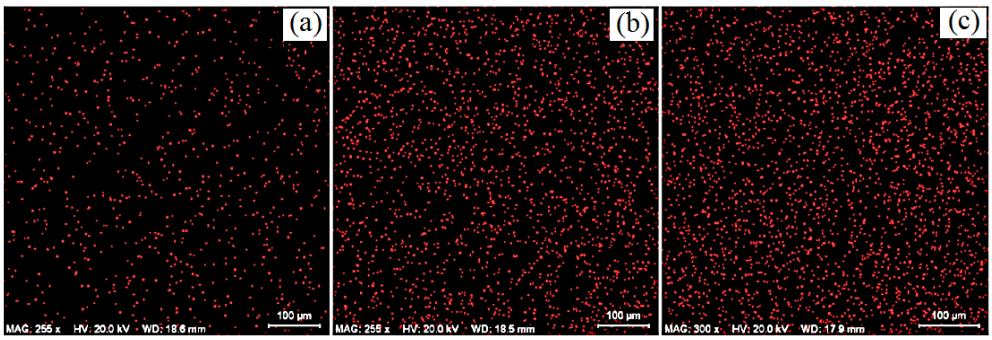

Fig. 5- Elemental analysis mapping of the surface of Haynes 25 superalloy showing the distribution of oxygen in (a) as-received sample, (b) one-pass UITed sample, and (c) three-pass UITed sample.

attributed this to the grain refinement, increased electron activity/penetration, increased nucleation sites for the oxide, and finally the rapid formation of a protective layer on the surface. They also reported the development of compressive surface residual stresses reduces the distance between atomic planes, increases the surface diffusion, and promotes the rapid growth of the surface layer. A decrease in corrosion resistance was also observed in UIT at supercritical pressures and was attributed to the increased tool-work surface friction and, accordingly, increased surface abrasion, material overlap, and increased roughness [18].

The formation of HCP-structured ε-martensite (with the higher defect density and greater internal strain) in the γ-FCC matrix of the alloy (Fig. 2b) causes microstructural heterogeneity and favors the galvanic corrosion [30]. However, the results suggest that at least up to one UIT pass, martensite formation has little effect on the corrosion resistance or even accelerates the formation of the passive film. Increasing the applied strains in the higher UIT pass numbers decreased the corrosion resistance which can be attributed to the increased fraction of ε-martensite and/or process-related surface defects.

FESEM images showing the surface macro-morphology of selected UITed samples as well as the atomic force microscopy images (within a dimension range of 5×5 μm) corresponding to the surface of as-received and selected UITed samples (xUIT28-0.08-0.1) are shown in Figs. 7 and 8, respectively. According to Fig. 7, an increase in the number of passes up to seven, increases the surface smoothness of samples. However, as shown on the macro-graphs 7c and 7d, after the three pass of UIT, micro cavities (pits) and microcracks are appeared on the surface. According to the atomic force microscopy images, the height of the asperities in the as-received sample (Fig. 8a) and seven-pass UITed (Fig. 8e) is significantly higher than that of the two-pass and three-pass UITed samples (Fig. 8c and 8d). This indicates that applying UIT up to three passes reduces the surface roughness but increases the roughness with further increasing the number of passes.

Comparing the corrosion resistance of 2UIT28-0.16-0.9 and 1UIT28-0.12-0.9 samples reveals that despite two-fold increase in the number of UIT passes and more than about 30% increase in the tool feeding rate of the former, no obvious difference exists between their corrosion resistances. Comparing the corrosion rate and corrosion current of 3UIT28-0.08-0.1 and 7UIT28-0.08-0.1 samples with those of 1UIT28-0.08-0.1 sample also implies an increase in the corrosion rate. In agreement with the previous findings [19], this can be related to the hardness saturation in the one-pass UITed sample. In fact, applying the first pass of the UIT, improves the corrosion resistance. However, further increasing the number of passes to three and seven, decreases the corrosion resistance, probably due to the increased the density of surface defects such as micro-cavities, microcracks, and increased roughness (Fig. 6c and 6d).

The results of the electrochemical impedance analysis on the as-received and selected UITed samples based on electrochemical impedance spectroscopy (EIS) are presented in the form of Nyquist and Bode plots in Fig. 9. According to the electrochemical impedance analysis in the form of Nyquist plot (Fig. 9a), the smallest semicircle diameter corresponds to the as-received and seven-pass UITed samples indicating their lower resistance to corrosion. However, one-pass and two-pass UITed samples (static pressure of 0.9 bar) have the largest semicircle diameter, indicating their highest corrosion resistance. One-pass UITed sample (static pressure of 0.1 bar) shows an average resistance to corrosion which is in agreement with the Tafel analysis results.

The changes in the total apparent resistivity (Z) in terms of the logarithm of frequency are shown as a bode curve in Fig. 9b. As can be seen, all samples show the same resistance at high frequencies. At high frequencies, an electric double layer is not formed and the circuit resistance becomes equal to the resistance of the SBF solution electrolyte. At very low frequencies, the circuit resistance is equal to the sum of the solution resistance and the resistance of the electric double layer (or circuit capacitor). Therefore, the polarization or corrosion resistance of samples, which is equal to the difference in circuit resistances at very high and very low frequencies, can be determined. At the frequency of 0.1 Hz, one-pass UITed sample (static pressure of 0.9 bar) shows the highest impedance and the as-received and seven-pass UITed samples show the lowest impedance. Also, the one-pass and two-pass UITed samples (static pressure of 0.1 bar) show an average resistance, which is in agreement with the previous experiments.

4. Conclusion

1- Applying UIT causes severe plastic deformation of the surface layers to a depth of about 100 μm and the formation of deformation bands and strain-induced HCP martensite phase up to a depth of 400 μm. The formation of an ultrafine grain structure and the development of compressive residual stresses in the surface layers are other effects of this process.

2- Based on the Tafel polarization analysis, one pass UIT with a static pressure of 0.1 and 0.9 bar reduces the corrosion current of the as-received sample from 16.4 μA/cm^2 to 1.3 μA/cm^2 and 18.2

μA/cm^2, respectively, and reduces the corrosion potential from -0.6 V to -0.7 V and -0.8 V. Also, the results of electrochemical impedance testing (Nyquist plot) indicate that the lowest corrosion resistance is related to the as-received and seven-pass UITed samples. The highest corrosion resistance is also related to the one-pass and two-pass UITed samples at a static pressure of 0.9 bar.

3- Increasing the corrosion resistance in UITed samples is seemingly due to increasing the dislocation density, decreasing the grain size, and development of residual stresses on their surface layers. This is because they are likely to increase the free energy/activity of the surface, promote surface oxidation, and encourage the formation of protective layer on the sample surface.

4- Considering the effectiveness of the UIT process, it is suggested to investigate the effect of sample thickness on the process performance, as well as the process effect on the fatigue strength of L-605 implants.

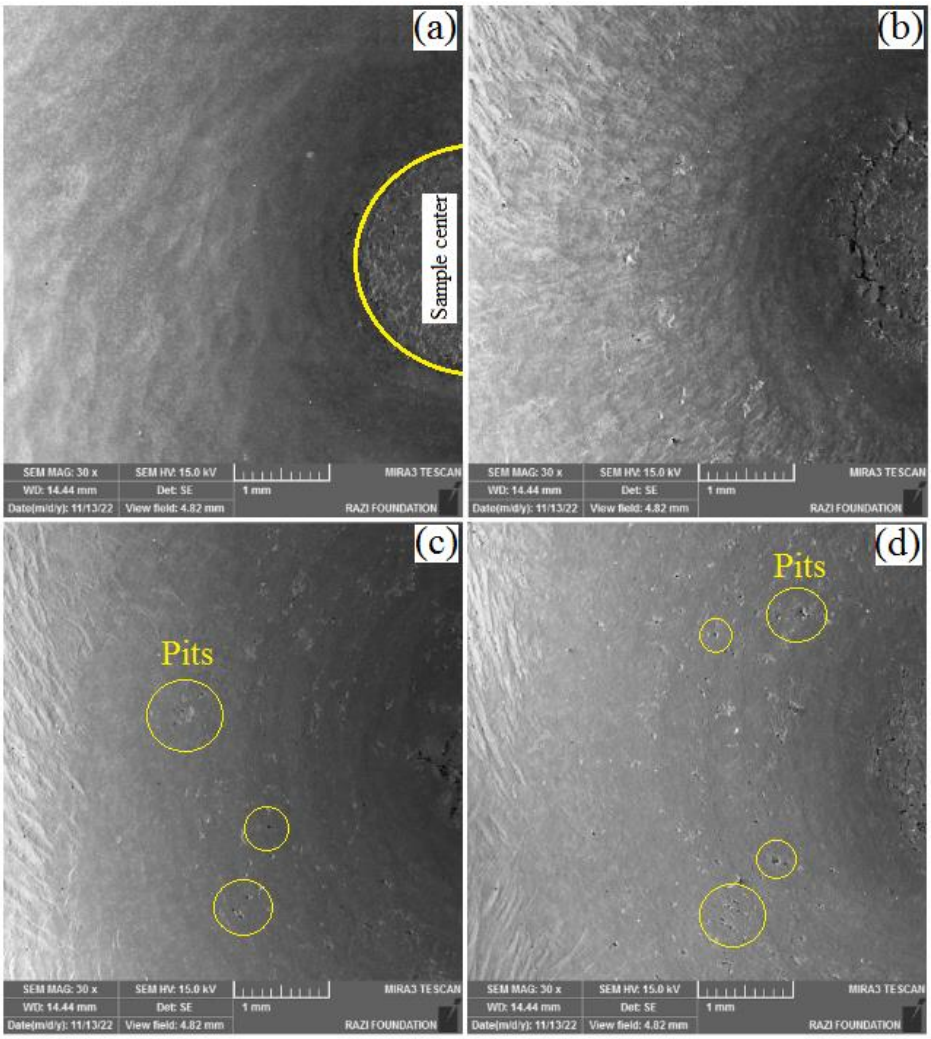

Fig. 7- FESEM images showing the surface macro-morphology of UITed samples (xUIT28-0.08-0.1) (a) one-pass UITed, (b) three-pass UITed, (c) five-pass UITed, and (d) seven-pass UITed. Some micro-cavities/microcracks are marked on the macrographs.

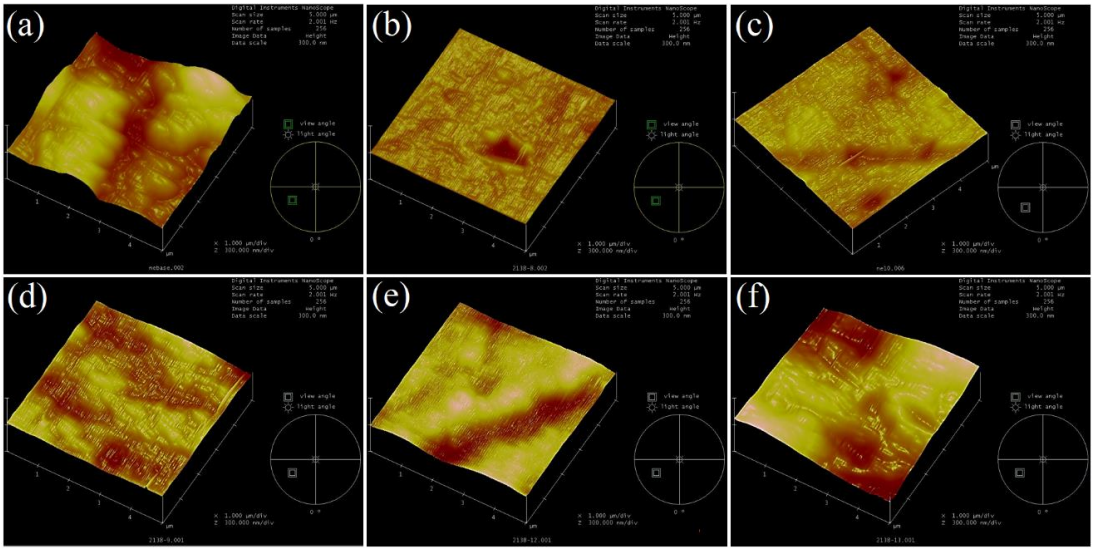

Fig. 8- Atomic force microscope images showing surface roughness of (a) as-received sample, and UITed samples xUIT28-0.08-0.1 (b) x=1, (c) x=2, (d) x=3, (e) x=5, and (f) x=7.

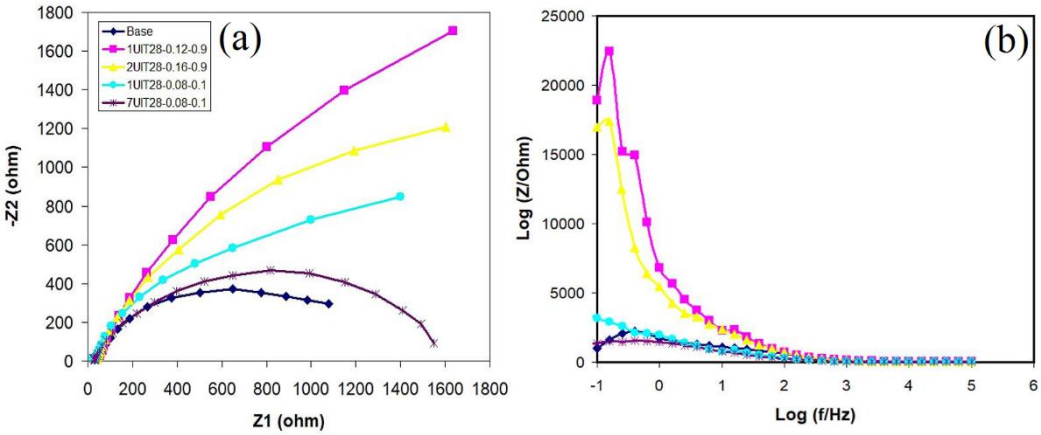

Fig. 9- Results of the impedance tests (a) Nyquist plot, (b) bode plot.

References

1. Mohanty CP, Chauhan AS. Exploring the machined surface characteristics of Haynes 25 superalloy: Cost mitigation and quality enhancement perspective. Surfaces and Interfaces. 2024;52:104912.
2. Yuan Q, Zhao H, Xi T, Yang C, Hao W, Yang K. Cold deformation behavior and microstructure evolution of biomedical Cu-containing L605 alloy. Journal of Alloys and Compounds. 2024;984:174005.
3. Catanio Bortolan C, Paternoster C, Turgeon S, Paoletti C, Cabibbo M, Lecis N, Mantovani D. Plasma-immersion ion implantation surface oxidation on a cobalt-chromium alloy for biomedical applications. Biointerphases. 2020;15(4).
4. Mohammadzehi S, Mirzadeh H. Grain refinement of austenitic stainless steels by cross rolling and annealing treatment: A review. Journal of Ultrafine Grained and Nanostructured Materials. 2024;57(2):112-9.
5. Yuan Y, Li R, Bi X, Yan M, Cheng J, Gu J. Review on numerical simulation of ultrasonic impact treatment (UIT): Present situation and prospect. Journal of Materials Research and Technology. 2024;30:1319-1340.
6. Asgari M, Honarpisheh M, Mansouri H. Experimental and Numerical Investigation of Mechanical Properties in the Ultrasonic Assisted constraint groove pressing process of copper sheets. Journal of Ultrafine Grained and Nanostructured Materials. 2020;53(1);48-59.
7. Cho IH, Song GH, Kim CS, Combs A, Park J, Suh CM, Park JH, Pyoun YS. Nano structured surface modification of tool steel and its beneficial effects in mechanical properties. Journal of mechanical science and technology. 2005;19:2151-2156.
8. Zaporozhets OI, Mordyuk BN, Mykhailovskyi VA, Halkina AA, Dordienko MO, Burmak AP, Langi E, Zhao LG. Tailoring elastic, mechanical and texture properties of Cu-37Zn brass by ultrasonic impact treatment applied at ambient and cryogenic temperatures. Materials Today Communications. 2024 Mar 1;38:108325.
9. Gu B, Yang Y, Wang Y, Lai J, Xu G, Gao L, Hu Y, Luo F. Study on the effects and mechanisms of ultrasonic impact treatment on impact toughness of Q345 steel welded joints. Engineering Fracture Mechanics. 2025;315:110754.
10. Gu B, Wang Y, Gao L, Xu G, Liu L, Sun S. Effects of ultrasonic impact treatment on the tensile properties of DH36 steel welded joints. Engineering Fracture Mechanics. 2025;315:110798.
11. Sebdani RM, Bilan HK, Gale JD, Wanni J, Madireddy G, Sealy MP, Achuthan A. Ultrasonic Impact Treatment (UIT) combined with powder bed fusion (PBF) process for precipitation hardened martensitic steels. Additive Manufacturing. 2024;84:104078.
12. Kavyani M, Ebrahimi GR, Ezatpour HR, Jahazi M. Microstructure refinement, mechanical and biocorrosion properties of Mg–Zn–Ca–Mn alloy improved by a new severe plastic deformation process. Journal of Magnesium and Alloys. 2022;10(6):1640-62.
13. Palumbo G, Thorpe SJ, Aust KT. On the contribution of triple junctions to the structure and properties of nanocrystalline materials. Scripta metallurgica et materialia. 1990;24(7):1347-1350.
14. Splinter SJ, Rofagha R, McIntyre NS, Erb U. XPS characterization of the corrosion films formed on nanocrystalline Ni–P alloys in sulphuric acid. Surface and Interface Analysis: An International Journal devoted to the development and application of techniques for the analysis of surfaces, interfaces and thin films. 1996;24(3):181-186.
15. Ralston KD, Birbilis N. Effect of grain size on corrosion: a review. Corrosion. 20101;66(7):075005.
16. Lee S, White HS. Dissolution of the native oxide film on polycrystalline and single-crystal aluminum in NaCl solutions. Journal of The Electrochemical Society. 2004;151(8):B479.
17. Petrov YN, Prokopenko GI, Mordyuk BN, Vasylyev MA, Voloshko SM, Skorodzievski VS, Filatova VS. Influence of microstructural modifications induced by ultrasonic impact treatment on hardening and corrosion behavior of wrought Co-Cr-Mo biomedical alloy. Materials Science and Engineering: C. 2016;58:1024-1035.
18. Kim KT, Kim YS. The effect of the static load in the UNSM process on the corrosion properties of alloy 600. Materials. 2019;12(19):3165.
19. Nemati R, Taghiabadi R, Yazdi MS, Amini S. Ultrasonic impact treatment of CoCrWNi superalloys for surface properties improvement. Materials Testing. 2025;67(2):372-385.
20. Favre J. Recrystallization of L-605 cobalt superalloy during hot-working process (Doctoral dissertation, INSA de Lyon; Tōhoku Daigaku (Sendai, Japon)).
21. Tao NR, Lu J, Lu K. Surface nanocrystallization by surface mechanical attrition treatment. Materials science forum. 2008;579;91-108.
22. Luna-Manuel JC, Lagar-Quinto S, Ramirez-Ledesma AL, Juarez-Islas JA. Thermomechanical and annealing processing effect on a rapid solidified Co–20 wt.% Cr alloy. Journal of Physics: Conference Series 2021;1723(1):012002.
23. Luo J, Wu S, Lu Y, Guo S, Yang Y, Zhao C, Lin J, Huang T, Lin J. The effect of 3 wt.% Cu addition on the microstructure, tribological property and corrosion resistance of CoCrW alloys fabricated by selective laser melting. Journal of Materials Science: Materials in Medicine. 2018;29:1-6.
24. Zhu ZY, Meng L, Chen L. Strain-induced martensitic transformation in biomedical Co–Cr–W–Ni alloys. Rare Metals. 2020;39(3):241-249.
25. Sembiring JP, Amanov A, Pyun YS. Artificial neural network-based prediction model of residual stress and hardness of nickel-based alloys for UNSM parameters optimization. Materials Today Communications. 2020;25:101391.
26. Abbasi A, Amini S, Shikhzade G. Investigation of experimental and numerical simulation of residual stresses distribution of rolling mill rolls in ultrasonic peening technology. Modares Mechanical Engineering. 2017;17(7):316-324.
27. Majidabad MA, Rezaei AR, Sabour MR, Faraji G. Mechanical properties and pitting corrosion behavior of Al5085 alloy processed via equal channel angular pressing (ECAP). Journal of Ultrafine Grained and Nanostructured Materials. 2023;1:9-14.
28. Sohrabi MJ, Dehghanian C, Mirzadeh H. Corrosion behavior of cold rolled and continuously heated SUS 304L stainless steel. Journal of Ultrafine Grained and Nanostructured Materials. 2024;57(1):19-27.
29. Chaudhari GP. Corrosion of nanostructured and ultrafine-grained metallic implant materials. Materials Technology. 2016 Nov 9;31(13):812-7.
30. Li ZX, Zhang LM, Udoh II, Ma AL, Zheng YG. Deformation-induced martensite in 304 stainless steel during cavitation erosion: Effect on passive film stability and the interaction between cavitation erosion and corrosion. Tribology International. 2022;167:107422.